9-14-2007

Ionic Winds for Locally Enhanced Cooling

David B. Go
Purdue University, dgo@purdue.edu

S V. Garimella
Purdue University, sureshg@purdue.edu

Timothy Fisher
tsfisher@purdue.edu

R. K. Mongia

Ionic winds for locally enhanced cooling

David B. Go, Suresh V. Garimella,[a] and Timothy S. Fisher
School of Mechanical Engineering and Birck Nanotechnology Center, Purdue University, West Lafayette, Indiana 47907, USA

Rajiv K. Mongia
Intel Corporation, 2200 Mission College Blvd, M/S RNB-6-53, Santa Clara, California 95054-1549, USA

(Received 7 March 2007; accepted 17 July 2007; published online 14 September 2007)

Ionic wind engines can be integrated onto surfaces to provide enhanced local cooling. Air ions generated by field-emitted electrons or a corona discharge are pulled by an electric field and exchange momentum with neutral air molecules, causing air flow. In the presence of a bulk flow, ionic winds distort the boundary layer, increasing heat transfer from the wall. Experiments demonstrate the ability of ionic winds to decrease the wall temperature substantially in the presence of a bulk flow over a flat plate, corresponding to local enhancement of the heat transfer coefficient by more than twofold. Multiphysics simulations of the corona and flow describe the ability of the ionic wind to distort a bulk flow boundary layer and confirm the experimentally observed heat transfer enhancement trends. © *2007 American Institute of Physics*. [DOI: 10.1063/1.2776164]

I. INTRODUCTION

As integrated circuits scale down, alternative technologies are required to cool local regions of high heat flux (i.e., "hot-spots"). Air cooling remains an attractive option for thermal management because of its cost advantages and relative ease of implementation. An increasing challenge in the future is that many components are expected to reach heat flux levels at which heat transfer augmentation will be required. Because it is impractical to add spreaders and heat pipes to these higher power components, there is a need for technologies where the heat transfer can be augmented without adding extra heat transfer area to the component. Microscale ionic winds can potentially enhance the bulk cooling of forced convection at the location of a hot-spot for more effective and efficient cooling. Because microscale ionic wind devices (i.e., "ionic wind engines") can be fabricated on an electronic chip, on a spreader, or on the skin of a notebook, they offer an attractive method for hot-spot thermal management.

Microscale ionic winds have been suggested previously as an air pumping technique for electronics cooling by Schlitz *et al.*[1] and Jewell-Larson,[2] but without detailed experimental evidence. Furthermore, because the air pumping device must also draw air through the entire electronic system, relying on ionic winds alone may be insufficient because they are often unable to generate the necessary pressure rise. In earlier work,[3] the use of ionic winds as a method of enhancing a preexisting bulk flow rather than as a method of pumping static air was modeled. In this configuration, a fan would still be used for cooling, and the ionic wind engines would be selectively placed in order to enhance heat transfer where required. Computational simulations at the continuum scale were conducted to explore the feasibility of this approach and indicated that a microscale ionic wind can enhance the local heat transfer coefficient of a 1 m/s bulk flow by approximately 50%.

For a device cooled by an external (i.e., fan-driven) bulk flow on its back side, an integrated ionic wind engine would be situated over a known hot-spot location and would consist of an electrode pair (anode and cathode) under an applied potential difference of the order of hundreds to thousands of volts, depending on the geometry. The configuration and spacing between the electrodes determine whether ions are generated by corona discharge or electron field emission. A corona is typically formed by a sufficiently high potential that is applied between a sharp electrode (a pin or wire) and a blunt, collecting electrode with an electrode gap separation of the order of millimeters. The geometrically enhanced electric field near the sharp electrode accelerates naturally occurring free electrons in the atmosphere so that they collide with neutral molecules. Recent work has suggested that as the gap decreases to ~ 10 μm or less, the impacting electrons are not naturally occurring, but tunnel from the surface of the cathode into the atmosphere.[4,5] In both cases, at sufficient kinetic energies, collisions between accelerated electrons and neutral air molecules strip an electron from the neutral molecule to form an ion. The ions are also accelerated through the atmosphere by the electric field, colliding with neutral molecules, exchanging momentum, and generating an ionic wind. The ionic wind acts as a secondary wind in the existing bulk flow, causing local fluid acceleration, and disrupts the velocity and thermal boundary layers to enhance the local cooling effect. Figure 1 depicts the concept of a chip-integrated ionic wind engine and demonstrates the principle of operation and the expected distortion of the local boundary layer due to the ionic wind.

Ionic wind flows generated by corona discharges were originally quantified by Chattock.[6] Stuetzer[7] and Robinson[8] published seminal works investigating the use of ion drag as pumps for both air and liquids. Since then, ionic winds have

[a]Author to whom correspondence should be addressed. Electronic mail: sureshg@ecn.purdue.edu

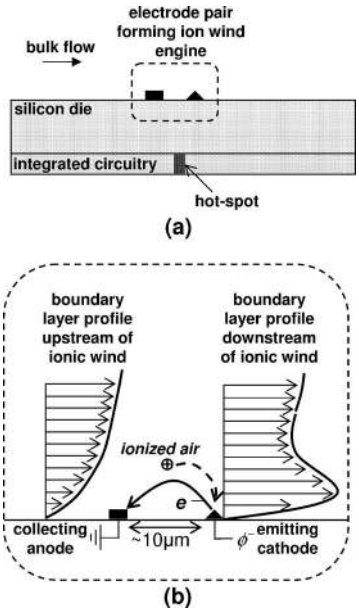

FIG. 1. (a) A schematic diagram of an ionic wind engine integrated on the back side of a chip cooled by an externally generated bulk flow. A local hot-spot is indicated on the active side of the chip. (b) Zoomed view demonstrates the principle of operation of the ionic wind engine and the distortion of the local boundary layer.

been investigated for applications ranging from blowers to air filtration and heat transfer enhancement. From a thermal perspective, a variety of corona configurations have been investigated including point-to-plane impingement,[9–11] pumping air in ductlike structures,[12] and enhancing internal flows.[13] The work of Molki and Bhamidipati[13] includes a comprehensive literature survey on corona discharges and corona winds for heat transfer enhancement.

The use of ionic winds in the presence of a bulk flow to modulate an external boundary layer has been an area of growing interest in the aerospace community. The concept was initially studied numerically by Rosendale *et al.*,[14] and Soetomo[15] conducted experiments on ionic winds in the presence of flat plate flows for drag reduction. His work was complemented by the numerical studies of El-Khabiry and Colver.[16] Recently Léger *et al.*[17]and Kimmel *et al.*[18] investigated and demonstrated the ability of corona discharges to reduce drag using electrodes perpendicular to the flow and either flush or in contact with a flat plate.

Little work exists on the heat transfer effects of ionic wind-enhanced external flow. The only reported experiments of which we are aware were performed by Velkoff and Godfrey[19] who used an array of corona wires aligned with the flow and extended above a flat plate, which also acted as the collecting electrode. They demonstrated an increase in the Nusselt number for low-velocity bulk flows but found that the impact of the ionic wind was minimal in the presence of high-velocity flows.

At the microscale, recent experimental and numerical work has also been completed by the authors' group. Peterson *et al.*[4] demonstrated electron emission in air for turn-on potentials on the order of tens of volts for 10 μm electrode gaps using surfaces enhanced by nanofabricated, polycrystalline diamond. Zhang *et al.*[5] used particle-in-cell/direct simulation Monte Carlo (DSMC) modeling to predict the ionization of air due to field-emitted electrons and breakdown voltages near 400 V for 10 μm electrode gaps. Additionally, Go *et al.*[20] used DSMC to predict field emission and ionization between two parallel electrodes in order to evaluate the effects of elevated electrodes in reducing ion trapping at the flat plate.

The purpose of the present work is to evaluate the efficacy of integrated ionic engines as a method of heat transfer enhancement and to present macroscale evidence of the ability of an ionic wind to enhance convective cooling.

II. EXPERIMENT

A. Methods

In order to demonstrate the phenomenon of ionic wind-enhanced heat transfer, macroscale experiments were conducted using corona discharges as the ion source. An axial fan was used as the bulk flow source, and 50.8 mm thick honeycomb with 3.175 mm cells was placed downstream of the fan to condition the flow prior to encountering the flat plate. The flat plate consisted of a glass plate, 0.7 mm thick, with a layer of indium tin oxide (ITO) on the back side. Electrodes were attached to the ITO layer, and a dc power supply was used to heat the glass plate resistively. On top of the plate, Teflon tape (0.127 mm thick) was used as a dielectric layer and painted with Krylon Ultra Flat Black Spray 1602, which has a known emissivity of 0.96.[21] The setup was placed on a Styrofoam block to insulate the back side of the glass plate and placed between parallel, polycarbonate plates used to duct the bulk flow. A 50 μm diameter, stainless steel wire was strung between the two polycarbonate plates and elevated 3.15 mm above the flat plate by ceramic blocks. A 6.35 mm wide strip of copper tape was used as the collecting electrode on the surface of the flat plate. Both corona electrodes were perpendicular to the bulk flow, and the corona wire was placed 54.6 mm downstream from the leading edge of the flat plate, while the collecting electrode was placed 3.8 mm downstream of the corona wire.

A large positive potential was applied to the corona wire using a high-voltage dc power supply, and the collecting electrode was grounded. A picoammeter was used to monitor the current passing through the collecting electrode. A FLIR ThermaCAM SC300 infrared (IR) camera was located above the glass plate with a plane perspective and recorded the transient temperature of the plate and, using a blackbody calibrator, was determined to have an accuracy of ± 1 °C over the range of 30–70 °C. The flow duct was open at the top to allow line of sight for the thermal imaging camera. Velocity measurements were obtained with a TSI Velocicheck 8330 hand-held velocimeter at the wire electrode to characterize the bulk flow in the area of interest. Multiple velocity measurements were obtained, and the measurements had an estimated uncertainty of ± 0.05 m/s.

B. Experimental results

Figure 2 shows thermal images of the flat plate for two different bulk velocities but identical corona operating conditions. The corona was operated at an applied potential of

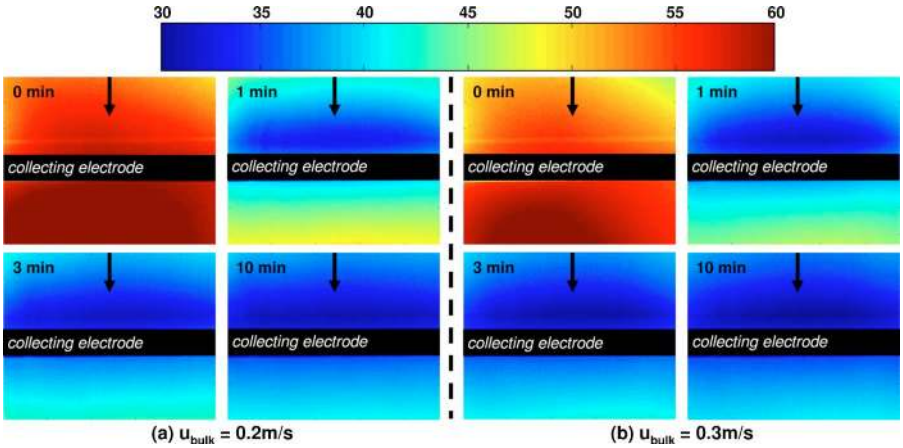

FIG. 2. (Color online) Thermal contours (in °C) at four different times during corona operation (i=51 μA, Φ=4575 V) in the presence of bulk flows of (a) 0.2 m/s and (b) 0.3 m/s. The upper left image is at 0 min, prior to corona activation but with a steady-state bulk flow condition. Subsequent images are at 1, 3, and 10 min after the corona was initiated, and the 10 min image represents a steady-state condition. The arrows indicate the direction of both the bulk flow and ionic wind, and the black strip indicates the collecting electrode.

Φ=4575 V producing a current of i=51 μA, and the bulk velocities were u_{bulk}=0.2 m/s and 0.3 m/s, respectively. The heat input was 4.3 W for all the work presented here. The images indicate that the maximum cooling occurs upstream of the collecting electrode in the vicinity of the corona wire. The observed maximum temperature decreases relative to baseline conditions (baseline defined as the absence of corona) were 27 °C for u_{bulk}=0.2 m/s and 25 °C for u_{bulk} =0.3 m/s. The images also show that the initial cooling occurs near the corona wire, but as the system approaches steady state, the ionic wind's influence impacts regions both upstream and downstream of the electrode pair.

Figure 3 shows the transient history of the average temperature between the corona wire and collecting electrode. In this time sequence, a bulk flow of 0.3 m/s was initiated at 5 min, and the corona (i=51 μA, Φ=4575 V) was activated at 30 min and then turned off at 50 min. The corona response is seen to be relatively fast, producing a steady condition in approximately 5 min. When the corona is deactivated, the plate recovers the steady-state, bulk-flow temperature in approximately 5 min. A slight disparity near t=31 min was due to local breakdown of air that was quickly corrected.

Temperature differences with the corona and without the corona were also characterized along the direction of the flow. Figure 4 shows the temperature differences under a steady corona condition relative to a steady bulk flow condition for four different corona powers in a 0.2 m/s bulk flow. Interesting characteristics in the thermal behavior are evident with varying corona current. At lower corona currents, upstream heating of a few degrees occurs, possibly due to Joule heating of the ions that diffuses upstream. As the corona current increases, the body force imparted on the flow by the ionic wind reduces upstream diffusion. Therefore, at higher corona currents the net effect is a cooling upstream of the corona wire caused by local induction of cooler fluid.

A second trend involves a shift in the location of the peak temperature difference as corona current increases. For lower corona currents, the cooling effect increases downstream of the corona wire, and the peak occurs just downstream of the collecting electrode. However, at higher cur-

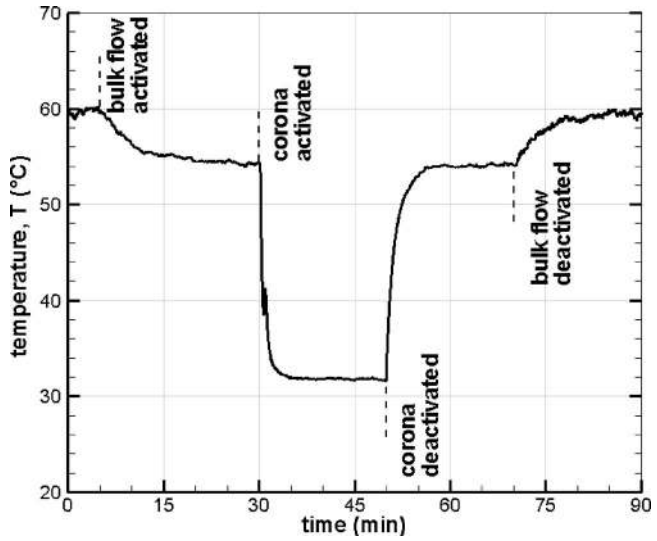

FIG. 3. Averaged surface temperature over the area between the corona wire and collecting electrode as a function of time. The bulk flow was initiated at 5 min and the corona was activated at 30 min. The corona was turned off at 50 min and the bulk flow was turned off at 70 min. The bulk flow was 0.3 m/s and the corona was operated at i=51 μA and Φ=4575 V.

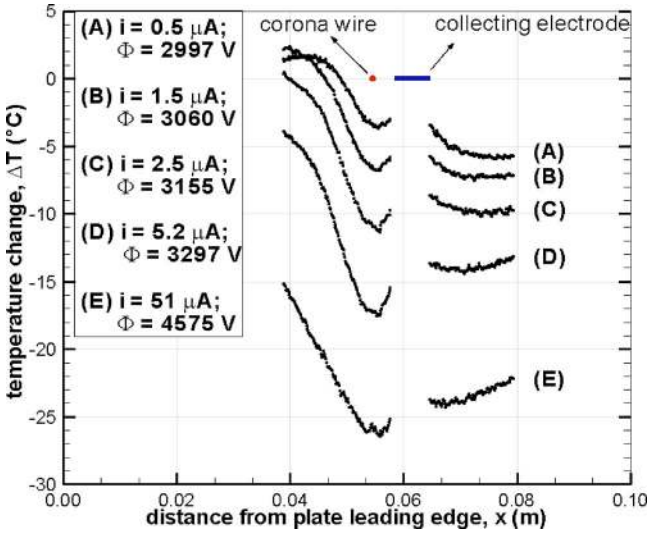

FIG. 4. (Color online) Temperature differences along the direction of flow for five corona conditions. The temperature difference is between a steady-state 0.2 m/s bulk flow condition and a steady corona condition. The solid dot and thick line represent the positions of the corona wire and collecting electrode, respectively.

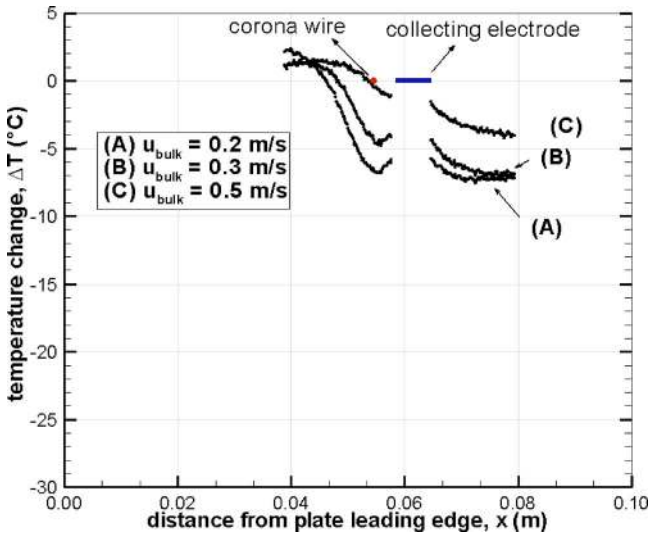

FIG. 5. (Color online) Temperature differences along the direction of flow between a steady-state bulk flow condition and steady corona condition of $i=1.5$ μA, $\Phi=3060$ V for various bulk velocities. The solid dot and thick line represent the positions of the corona wire and collecting electrode, respectively.

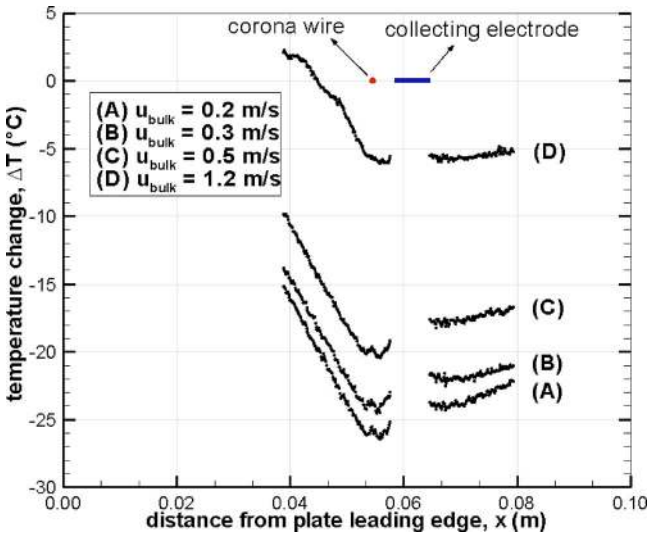

FIG. 6. (Color online) Temperature differences along the direction of flow between a steady-state bulk flow condition and steady corona condition of $i=51$ μA, $\Phi=4575$ V for various bulk velocities. The solid dot and thick line represent the positions of the corona wire and collecting electrode, respectively.

rents the largest temperature drop occurs in the vicinity of the corona wire and decreases downstream of the collecting electrode.

A third observation concerns the relative impact of the ionic wind. When the corona current is increased by an order of magnitude (case *A* to *D*), the temperature drop only increases by a factor of 4, and when the corona current increases by two orders of magnitude (case *A* to *E*) the temperature drop at the wire only increases by a factor of 6.5. One might expect that increasing the corona current by orders of magnitude would increase the body force and produce a similar effect on heat transfer. However, two reasons exist to explain why the relative impact on heat transfer is moderate. First, Joule heating of the air by the corona current also increases with corona current and decreases the relative heat transfer between the flow and the flat plate, though this effect is likely small based on the ratio of heater power to corona power. Second, the relationship between flow and heat transfer is not linear. Based on a laminar flow, flat plate assumption, the heat transfer rate should be proportional to the fourth-root of ion concentration.[3,9]

Based on the foregoing observations, we cannot conclusively ascertain whether the observed effects are due to the magnitude of the corona alone, or the interaction of the corona and the bulk flow. Figures 5 and 6 show axial plots for different bulk velocities at two different constant corona powers. Figure 5, with velocities of 0.2, 0.3, and 0.5 m/s in conjunction with a corona current of 1.5 μA, shows that as bulk velocity increases, the enhancement in the vicinity of the corona wire decreases but the downstream trend is largely unaffected, although the downstream temperature drops decrease in magnitude. A similar trend is seen in Fig. 6 for bulk velocities of 0.2, 0.3, 0.5, and 1.2 m/s with a corona current of 51 μA. For this larger corona current, the magnitude of the localized body force is such that the downstream temperatures increase with streamwise position within the recorded temperature field because of the large up-stream enhancement compared to the prevailing conditions provided by the bulk flow.

III. NUMERICAL SIMULATIONS

A. Governing equations

To provide further insights into the observed enhancement, we have performed numerical simulations of the electrohydrodynamics and heat transfer. The transport of ions is governed by two fundamental equations. The electric and potential fields are defined by Poisson's equation as

$$\nabla \cdot \mathbf{E} = -\nabla^2 \Phi = \frac{\rho_e}{\varepsilon}, \tag{1}$$

where ρ_e is the ion concentration (C/m^3) and ε is the permittivity of air (8.85×10^{-12} F/m). Ion transport occurs by four mechanisms; conduction through the air; drift through the air, convection due to the bulk flow, and diffusion. The transport equation is therefore

$$\nabla \cdot (\sigma \mathbf{E} + b\mathbf{E}\rho_e + \mathbf{u}\rho_e) = D_{IA}\nabla^2 \rho_e. \tag{2}$$

Typically, the conduction term is negligible due to the extremely low electrical conductivity of air (1.61×10^{-23} Ω^{-1} m^{-1} and decreasing with temperature), and it was neglected in this work. The ion mobility in air is taken to be $b=3.0\times10^{-4} m^2/V$ s, and the mass diffusion coefficient is assumed to be that of O_2 in air at room temperature, $D_{IA}=2.0\times10^{-5} m^2/s$. Often, the convection term is dominated by drift terms due to high ion velocities relative to the bulk flow, and convection was assumed negligible. Ion drag is defined by a body force on the bulk flow as

$$\mathbf{f} = \rho_e \mathbf{E} - \frac{1}{2}|E|^2 \nabla \varepsilon + \frac{1}{2}\nabla\left[|E|^2 \rho \frac{\partial \varepsilon}{\partial \rho}\right]. \quad (3)$$

The three terms on the right side represent the Coulombic force, the force due to the permittivity gradient, and the electrostriction force, respectively. In general, the permittivity gradient is negligible [variation for air is less than 0.1% over a range of 1000 K (Ref. 22)]. Additionally, electrostriction does not affect the flow field in the absence of a two-phase interface.[11] Therefore, these two terms were neglected, and the body force was simply modeled as a function of the electric field and ion charge density. Negative ions are typically electrons and, due to their low mass, have a negligible effect on the bulk flow.

The bulk flow is steady and laminar and is governed by the following three equations:

$$\text{Continuity:} \quad \nabla \cdot (\rho \mathbf{u}) = 0; \quad (4)$$

$$\text{Momentum:} \quad \nabla \cdot (\rho \mathbf{u}\mathbf{u}) = -\nabla p + \nu \nabla^2 \mathbf{u} + \rho_e \mathbf{E}; \quad (5)$$

$$\text{Energy:} \quad \mathbf{u} \cdot \nabla(\rho C_p T) = k\nabla^2 T + b\rho_e E^2 - \mathbf{u} \cdot (\rho_e \mathbf{E}). \quad (6)$$

The second term on the right side of Eq. (6) is the Joule heating energy source caused by the ion current.[11] However, not all ion energy is converted to heat because the ions do kinetic work on the bulk flow. Therefore the third term subtracts the kinetic work of the ions to account for this process. Because the local heating can affect the local air density, the ideal gas law was used to calculate ρ.

Equations (1), (2), and (4)–(6) were solved in a two-dimensional domain using the commercial finite volume software Fluent.[23] The ion transport and Poisson equations were solved using a generic scalar transport solver, whereas the flow and energy equations were solved with standard solvers. Because Eqs. (1) and (2) are decoupled from the flow equations, they were solved first, followed by the flow equations. A nonuniform mesh was used with increased mesh densities near the leading edge, in the boundary layer region above the plate, and in the vicinity of the electrodes. The corona wire electrode was modeled explicitly as a solid region in the flow domain, and the collecting electrode was modeled as a 6.35 mm section of the flat plate.

B. Boundary conditions

The flow was modeled as standard boundary layer flow in which the inlet velocity is uniform, and the plate was modeled as a no-slip, constant heat flux surface. Upstream of the flat plate, a symmetry condition (zero normal gradients) was used to ensure numerically uniform flow prior to the leading edge. The far field was also modeled as a symmetry boundary condition and set at a height ten times the expected boundary layer thickness at the domain exit.

Two standard boundary conditions exist for the Poisson equation. A specified potential value (Dirichlet condition) is used at the collecting electrode and corona wire. The collecting electrode was grounded and modeled with a zero value, while the corona wire was given the applied potential (Φ). All other portions of the flat plate were assumed to be insulating due to the dielectric Teflon tape in the experiment.

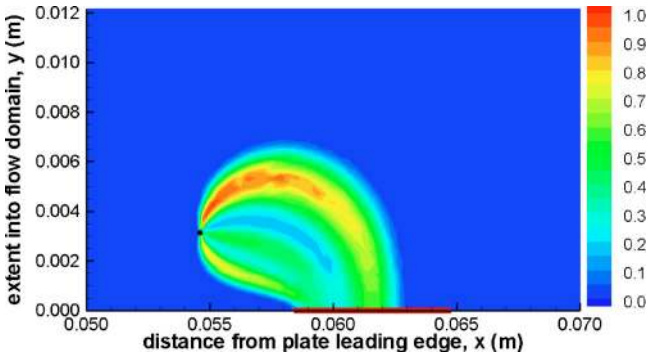

FIG. 7. (Color online) Simulated ion concentration contours (normalized) for a corona of $i=0.5$ μA, $\Phi=2997$ V. The corona wire is represented by the small black spot, and the red horizontal line on the boundary represents the collecting electrode.

Therefore, these boundaries were specified to have zero flux (Neumann condition), ensuring that the electric field normal to the surface was zero. The inlet and the outlet of the domain were also given zero flux boundaries, thus enforcing zero normal electric fields at those locations.

The ion transport equation was also modeled with two types of boundary conditions. The ion current density to a surface is defined as

$$j = bE_{\hat{n}}\rho_e. \quad (7)$$

No current flows to the dielectric surface, and this condition was specified implicitly by the zero flux boundary condition for the Poisson equation (zero normal electric field). The ion transport equation was also given a zero flux boundary condition to specify that ions cannot diffuse across the dielectric surface. The collecting electrode was given a zero flux boundary condition as well, but because the Poisson equation was set to zero in this region, the normal component of the electric field allows ion current into the collecting electrode but not ion diffusion across the electrode.

Corona discharges occur due to the enhanced electric field near the corona wire. The enhanced field ionizes the air in very close proximity to the wire. Because all ionization occurs very close to the boundary, the volume of the ionization region was assumed negligible, and an ion concentration value was specified at the boundary. The ion concentration at the corona wire was varied until the simulated current at the collecting electrode, as defined by Eq. (7) matched the experimental value.

C. Numerical results

In order to compare the numerical simulations to the experiments, the simulations used hydrodynamic and thermal boundary conditions consistent with the experimental conditions. For all subsequent results, the bulk flow velocity was 0.2 m/s, and the heating power at the wall was 4.3 W. Figure 7 shows normalized ion concentration contours for a simulated corona with $i=0.5$ μA and $\Phi=2997$ V. The shape of the ion cloud follows that of the electric field due to the applied potential. The ion current also concentrates on the front half of the collecting electrode, where the electric field is strongest.

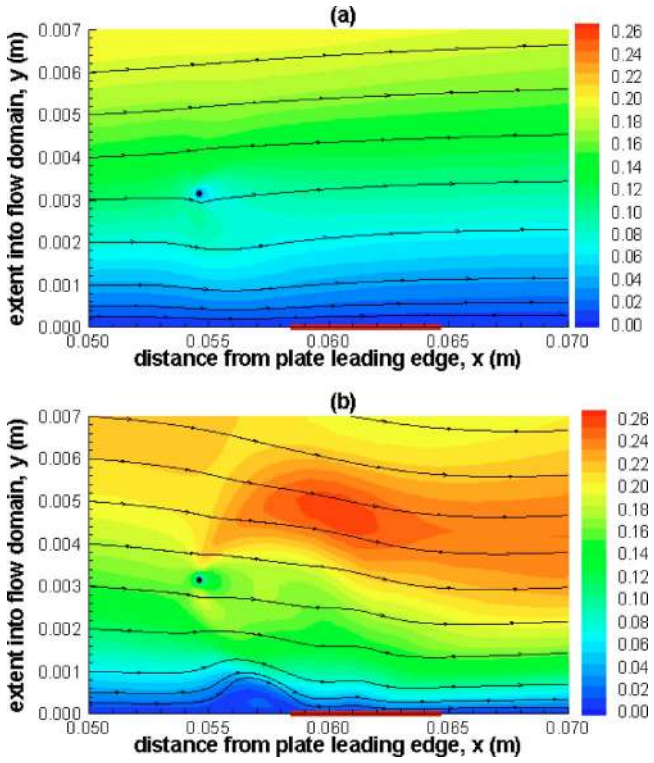

FIG. 8. (Color online) Velocity magnitude contours (in m/s) and streamlines for (a) 0.2 m/s bulk flow with no corona and (b) 0.2 m/s bulk flow with a corona of $i=0.5$ μA, $\Phi=2997$ V. The corona wire is represented by the small black spot and the red horizontal line on the boundary represents the collecting electrode.

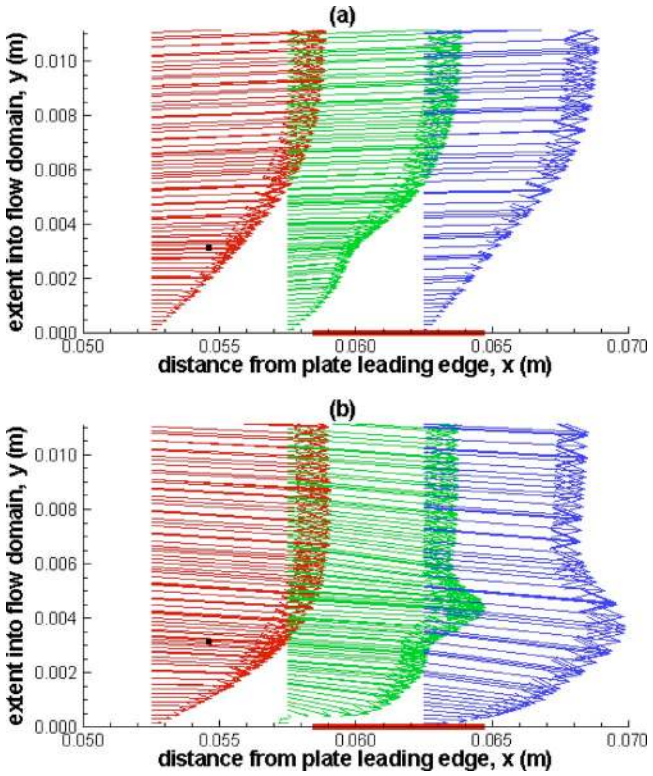

FIG. 9. (Color online) Normalized velocity vectors for (a) 0.2 m/s bulk flow with no corona and (b) 0.2 m/s bulk flow with a corona of $i=0.5$ μA, $\Phi=2997$ V. The corona wire is represented by the small black spot and the red horizontal line on the boundary represents the collecting electrode.

Figure 8 shows velocity magnitude contours and streamlines from the numerical simulation for a bulk flow of 0.2 m/s with and without the corona described above. Comparison of Figs. 8(a) and 8(b) reveals that the velocity between the wire and collecting electrode nearly doubles in magnitude due to the ionic wind. The streamlines also demonstrate how the flow is pushed toward the collecting electrode by the ionic wind. Because the corona wire is elevated above the collecting electrode, the ionic wind velocity contains a y-component as well as an x-component. The y-component serves to thin the boundary layer by pushing the flow closer to the surface, whereas the x-component locally accelerates the streamwise flow.

Figure 9 contains velocity vector plots at three locations in the flow that clearly demonstrate how the flow is accelerated by the ionic wind. At all three locations, upstream (furthest left), between the electrodes (middle), and downstream (furthest right), the flow without an active corona resembles standard boundary layer flow with slight distortion due to the presence of the corona wire. In Fig. 9(b), the upstream location does not exhibit significant distortion near the wall, but the entire profile is accelerated due to a funneling effect through which the ionic wind increases mass flow through the region. The velocity profile between the electrodes reveals significant acceleration and distortion and very near to the wall shows some recirculation as the flow appears to separate slightly. The downstream profile resembles that shown in the schematic in Fig. 1(b), whereby the near-wall flow is accelerated to speeds greater than the freestream flow. While the corona does not extend all the way to the downstream location, the kinetic energy added to the flow is maintained downstream of the corona until it dissipates into the freestream. All three vector diagrams indicate that the ionic wind does induce a slight negative velocity in the y-direction, pushing the boundary layer closer to the wall as discussed above. However, the effect is small in comparison to the overall acceleration in the x-direction.

In order to compare the thermal effects of the corona, a nondimensional wall temperature is defined as

$$\theta = \frac{T_{\text{wall, no corona}} - T_\infty}{T_{\text{wall, corona}} - T_\infty}, \tag{8}$$

where the bulk flow temperature T_∞ is a defined parameter, and the local wall temperatures are extracted from the simulation. The parameter θ defines the ratio of the thermal driving potential at the wall with and without corona. The wall temperatures are also known from the infrared images, and a similar quotient can be calculated for the experiments. Figure 10 shows a comparison between the simulation and the experiment for two corona conditions in 0.2 m/s flow. As indicated in the figure, the simulation captures major trends of the temperature variation, such as a peak temperature drop at the corona wire. The slight offset between the simulations and experiments can be attributed to the uncertainty in the x-position of the experimental data. Because these data are extracted from a pixilated IR image, there is approximately 1 mm uncertainty in x-locations (corresponding to 0.01 in nondimensional distance along the flat plate) Additionally, the

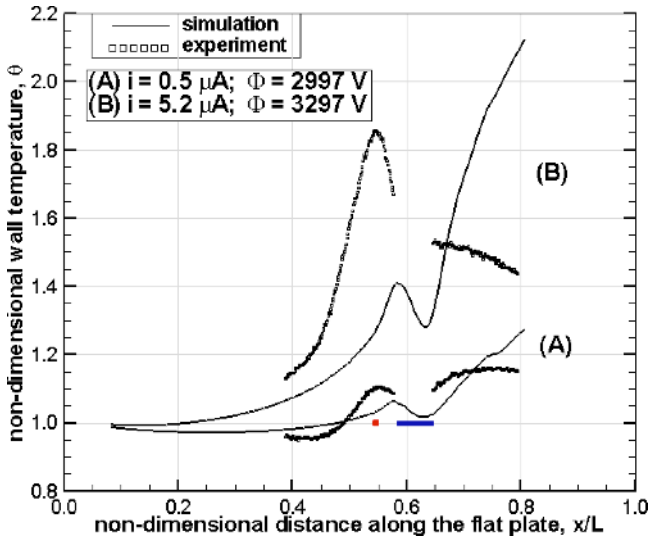

FIG. 10. (Color online) Comparison of the measured and predicted nondimensional temperature for a bulk flow of 0.2 m/s and two corona conditions. The solid dot and thick line represent the positions of the corona wire and collecting electrode, respectively.

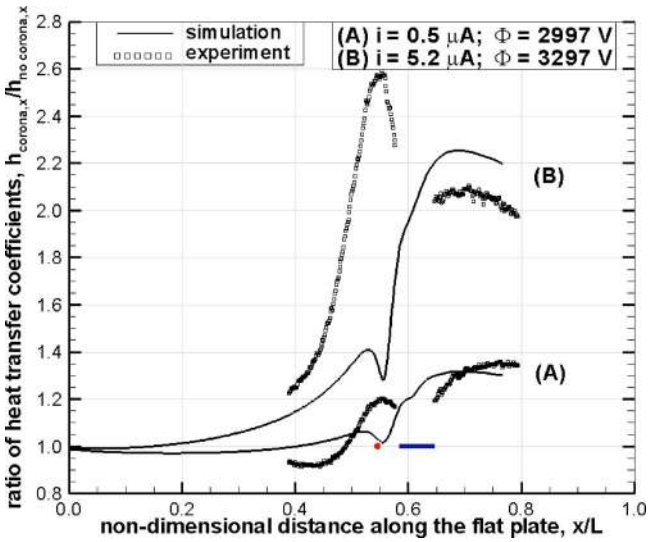

FIG. 11. (Color online) Comparison of the measured and predicted change in heat transfer coefficient for a bulk flow of 0.2 m/s and two corona conditions. The solid dot and thick line represent the positions of the corona wire and collecting electrode, respectively.

simulation correctly predicts the occurrence of upstream heating ($\theta<1$) for the low-power corona ($i=0.5$ μA) as well as the absence of the upstream heating for the high power corona ($i=5.2$ μA).

The heat transfer performance of the corona can be characterized by the change in the local heat transfer coefficient. The local heat transfer coefficient from the experimental results is calculated based only on the heat lost to convection (by subtracting the radiation component) as follows:

$$h_x = \frac{q''_{\text{heater}} - q''_{\text{wall, radiation}}}{T_{\text{wall, }x} - T_\infty}. \tag{9}$$

Figure 11 shows the ratio of heat transfer coefficient for bulk flow with and without corona for two conditions. For the low corona power condition of 0.5 μA and 2997 V, the simulation matches the trends relatively well. For the high power condition of 5.2 μA and 3297 V, the simulation again captures the trends, although it underpredicts the relative magnitude of the peak near the corona wire. However, it does indicate the absence of upstream heating as observed in the experiment. Both simulations predict a gradual decrease in heat transfer coefficient downstream of the electrodes due to the dissipation of the additional kinetic energy added to the flow by the ionic wind. The heat transfer enhancement can be attributed to the boundary layer and velocity distortion illustrated in Figs. 8 and 9. The flow is accelerated between the electrodes, and the boundary layer is thinned, thereby bringing cooler, freestream air closer to the wall to enhance cooling.

Figures 10 and 11 both reveal some discrepancy between simulations and experiments in the magnitude of local enhancement for the high-power corona condition. Because the simulations are two-dimensional, they do not capture all effects of 3D experiments or nonuniformities in the corona or flow. Additionally, the flat plate is modeled as a perfect dielectric and is therefore assumed to be perfectly insulating. In the experiment, however, the flat plate was a thin glass sheet with a metallic heater layer on the back side. The glass plate had a floating potential and, when the applied voltage was at higher values, there may have been some ion flow directly to the glass plate in addition to the collecting electrode. The additional discharge region would increase the area over which the ionic wind acts and result in impingement directly beneath the corona wire. The increased corona area and impingement at higher powers would produce an increased local effect but little downstream effect because the x-component of the ionic wind would be largely unchanged. However, the imperfect dielectric effect is not modeled in the simulations, which required all current to flow between the cathode and anode. In general, however, the simulations do add insights regarding the local interactions between the corona and the bulk flow near the heated surface.

IV. CONCLUSIONS

In this work, the concept and principle of operation for ionic wind engines have been presented as a method of localized air cooling. Experiments using corona discharges have demonstrated local cooling enhancement of bulk flows due to ionic winds. With ionization, a more than twofold enhancement of the local heat transfer coefficient was observed in the presence of typical externally forced flow conditions. Multiphysics simulations of the corona and flow describe the ability of the ionic wind to distort a bulk flow boundary layer and confirm experimentally observed heat transfer enhancement trends. Future work will include establishing relationships between the flow, corona power, and cooling enhancement and will extend the study to microfabricated ionic wind engines that operate via electron field emission.

ACKNOWLEDGMENTS

The authors wish to thank Dan Schlitz of Thorrn Micro Technologies for useful discussions on the numerical simulations. Financial support and technical insights from Intel Corporation are also acknowledged.

[1]D. J. Schlitz, S. V. Garimella, and T. S. Fisher, *Proceedings of the ASME Heat Transfer/Fluids Engineering Summer Conference*, Charlotte, NC, 2004 (American Society of Mechanical Engineers, New York, 2004), Paper No. HT-FED04–56470.
[2]N. E. Jewell-Larsen, M.S. thesis, University of Washington, 2004.
[3]D. B. Go, S. V. Garimella, and T. S. Fisher, *Proceedings of the Tenth Intersociety Conference on Thermal and Thermomechanical Phenomena in Electrical Systems*, San Diego, CA, 2006 (Institute of Electrical and Electronics Engineers, New York, 2006).
[4]M. S. Peterson, W. Zhang, T. S. Fisher, and S. V. Garimella, Plasma Sources Sci. Technol. **14**, 654 (2005).
[5]W. Zhang, T. S. Fisher, and S. V. Garimella, J. Appl. Phys. **96**, 6066 (2004).
[6]A. Chattock, Philos. Mag. **48**, 401 (1899).
[7]O. Stuetzer, J. Appl. Phys. **30**, 984 (1959).
[8]M. Robinson, AIEE Trans. **80**, 143 (1961).
[9]K. G. Kibler and H. G. Carter, Jr., J. Appl. Phys. **45**, 4436 (1974).
[10]B. L. Owsenek, J. Seyed-Yagoobi, and R. H. Page, J. Heat Transfer **117**, 309 (1995).
[11]B. L. Owsenek and J. Seyed-Yagoobi, J. Heat Transfer **119**, 604 (1997).
[12]H. Kalman and E. Sher, Appl. Therm. Eng. **21**, 265 (2001).
[13]M. Molki and K. L. Bhamidipati, Int. J. Heat Mass Transfer **47**, 4301 (2004).
[14]J. R. Rosendale, M. R. Malik, and M. Y. Hussaini, AIAA J. **26**, 961 (1988).
[15]F. Soetomo, M.S. thesis, Iowa State University, 1992.
[16]S. El-Khabiry and G. M. Colver, Phys. Fluids **9**, 587 (1997).
[17]L. Léger, E. Moreau, and G. Touchard, IEEE Trans. Ind. Appl. **38**, 1478 (2002).
[18]R. L. Kimmel, J. R. Hayes, J. A. Menart, and J. Shang, *Proceedings of the AIAA 42nd Aerospace Sciences Meeting*, Reno, NV, 2005 (American Institute of Aeronautics and Astronautics, Washington, DC, 2005), Paper No. AIAA2004–509.
[19]H. R. Velkoff and R. Godfrey, J. Heat Transfer **101**,157 (1979).
[20]D. B. Go, T. S. Fisher, and S. V. Garimella, *Proceedings of the ASME International Mechanical Engineering Congress and Exposition*, Chicago, IL, 2006 (American Society of Mechanical Engineers, New York, 2006), Paper No. IMECE2006–14476.
[21]NASA, 2003. Data on the emissivity of a variety of black paints. http://masterweb.jpl.nasa.gov/reference/paints.htm (accessed 22 August 2006).
[22]E. W. Washburn, *International Critical Tables of Numerical Data, Physics, Chemistry and Technology, 1st Electronic Edition* (Knovel, Norwich, NY, 2003), pp. 1926–1930.
[23]Fluent Inc., Fluent 6.1 User's Guide, Lebanon, NH, 2003.